Chapter 02

A meso-scale model to predict flow stress and microstructure during hot deformation of IN718WP

Abstract: This chapter presents a dislocation-based hot deformation model to address a nickel-based superalloy's flow stress response and discontinuous dynamic recrystallization (DDRX) behavior. The developed model can predict the flow curves and subsequent microstructure evolutions during the hot deformation. The evolution of microstructure-reliant internal variables was predicted and validated thoroughly. Furthermore, the influence of strain rate and temperature on the glide and climb velocities have also been discussed to reveal more insights into the microstructural development. Dislocation density and DDRX fraction predicted from the model was compared with dislocation density and DDRX fraction obtained from electron backscattered diffraction (EBSD) measurements with reasonable matching. Higher temperatures and slower strain rates provide favorable conditions for DDRX in this alloy. The importance of this model relies on its prediction capability in terms of flow curve, mobile and immobile dislocation densities, DDRX fraction, grain size and dislocation velocities. Single set of parameters were obtained from 12 experimental curves and rest of the 11 curves were predicted by the model using those parameters. The approach used in the present chapter is helpful to reduce the experiments and can predict multiple flow curves along with the corresponding microstructure evolution.

2.1. Introduction

Mean-field physical modelling of flow stress provides a mathematical framework to comprehend the deformation behavior of alloys and establish the relation between their microstructure and flow properties. Based on the material and microstructure, internal state variables, material constitutive

parameters and constants are used in the development of the deformation model. The selection of the of these parameters are physically based and representing the reality, as bulky models with a large number of parameters in non-linear equations can make interpretation very difficult [67-70] . As flow stress is a crucial parameter in understanding thermomechanical processes such as extrusion, rolling, forging, and other manufacturing processes, its modelling depends on complex microstructures that enable the definition of internal variables. The processes mentioned above include strain hardening (SH), dynamic recovery (DRV) and dynamic recrystallization (DRX) mechanisms [71]. Furthermore, DRX is divided into three categories: geometric dynamic recrystallization (GDRX), continuous dynamic recrystallization (CDRX), and discontinuous dynamic recrystallization (DDRX) [72]. Phenomena such as GDRX leads to the replacement of the original grains through deformed elongated grains due to an appreciable reduction in one direction during metalworking processes [73]. CDRX involves the transformation of low-angle grain boundaries (LAGBs) to high-angle grain boundaries (HAGBs), and it is generally observed during the hot deformation of high stacking fault energy materials, such as aluminum [74], Magnesium alloys [75-77], RAFM steel [12] and titanium alloys [78]. DDRX involves the nucleation and growth of new grains at the expense of the deformed materials, and it occurs during the hot deformation of low stacking fault energy materials, such as OFHC copper [79], austenitic stainless steels [80, 81], Ni-Co alloy [82] and nickel-based superalloys [29, 64]. In this work we have focused on nickel-based superalloy because it is widely used in the hot sections of power plants and aero engines [83, 84], where hot working/thermomechanical processing is a mandatory step. Researchers have focused on investigating and modelling the DDRX mechanism in Ni-based superalloys, which not only helps optimize the conditions for thermomechanical processes such as

rolling and forging but also enables better control over grain structure through best hot-working route [85].

During initial efforts, the flow stress models were associated with thermomechanical processing parameters such as temperature, strain and strain rate[70, 86, 87]. Thus, the physics behind microstructural evolution and deformation mechanisms could not be addressed [32, 88]. These models [32, 88] require many calibration parameters. By invoking the concept of DRV, SH and DRX [29, 30, 64], dislocation density-based models were developed to establish the correlation between flow stress response and microstructure evolution. Generally, these approaches consider the flow response as, $\sigma_{flow} = f(\rho \; and \; g)$, where ρ is dislocation density and g is grain size. The dislocation densities such as mobile and immobile dislocation density are considered as internal variables. The model proposed by [88] studied the stress-strain response in α-Fe containing interstitial atoms. Similarly, the dislocation density-reliant constitutive model has been developed and validated with copper [32], silver [32], titanium [89] and aluminum [32, 74].

The influence of deformation temperature, grain size and strain rate on the flow stress response has been discussed thoroughly for high stacking fault energy materials. Buzolin et al. [78] model predicted the substructure size, dislocation density and grain size during the hot deformation for TI5553 alloy. Lindgren et al. [34, 37] proposed a flow stress model for 316 L steel and predicted the evolution of solute and vacancy concentration during the deformation. In addition to flow stress and dislocation density evolution was also studied [34, 37]. Moretti et al. [5] proposed model for alloy 718 that considers the recovery due to cross slip of screw dislocation, phonon, and electron drag effect for high strain rate/temperature deformation.

While the reorganization of dislocations approaches work very well to describe plastic flow in high-stacking fault energy materials, even for heterogeneous deformation [90], they need some modifications to deal with low-stacking fault materials undergoing DDRX. Fisk et al. [3] proposed the model for 718 alloys that was capable to simulate the flow stress response for both, fully aged and annealed state materials. Lin et al. [29] developed a model for nickel-based superalloys that considers the evolution of grain size and its influence on grain boundary strengthening. This model [29] addressed the impact of recrystallized grain size on the WH and dynamic softening. Furthermore, Tang et al. [30] proposed a model for Ni-based superalloy that correlates the temperature and strain rate on the thermal stress component of flow stress. Yadav et al. [41] proposed a physical model to predict the deformation behavior in 304HCu. The effect of the strain rate and the deformation temperature on the substructure evolution was discussed. The model by Joseph et al. [91] incorporated the twin boundary strengthening concept [34, 37] to study the deformation behavior of Monel 400. Other than these models, efforts were also made employing cellular automata to deal with flow response and microstructures evolution [92, 93].

As per the literature survey of LSFE materials it can be deduced that, some of the developed models [4, 5, 34, 37, 63] predict the flow stress response nicely for relatively small strains but the microstructural development during deformation is not addressed properly. Other existing models [79, 85, 94] predicts the microstructure evolution along with flow stress response and the DDRX behaviour was also addressed. Similarly, some existing models [29, 30, 64, 95] were developed that addresses the hot deformation in a solid solution strengthening alloys with consideration of DDRX mechanism, but the insights from dislocation velocity and its relation with DDRX was not provided. Similarly, two internal variable based model that is more realistic with respect to the actual dislocation configurations in LSFE materials is a need [30, 34].In this work we have focused

on nickel-based superalloy because it is widely used in the hot sections of power plants and aero engines [83, 84], where hot working/thermomechanical processing is a mandatory step. Researchers have focused on investigating and modelling the DDRX mechanism in Ni-based superalloys, which not only helps optimize the conditions for thermomechanical processes such as rolling and forging but also enables better control over grain structure through best hot-working route [85].

This leads to the main objective of this chapter: the development of the dislocation-based flow stress model by invoking the concept of DDRX, DRV and SH for a nickel-based superalloy free of precipitates. Internal variables such as $\rho_{m,}$ and ρ_i have been incorporated into the model, and the flow stress response was modeled with a single set of parameters. In addition, EBSD was used to validate the dislocation density and DDRX fraction predicted by the model. The evolution of other variables, glide velocity and climb velocity was also discussed.

2.2. Materials and Methods

The chemical composition of the studied nickel-based superalloy is an Inconel®718 modified to avoid precipitation. The alloy is called IN718WP (WP: without precipitate), and its chemical composition is shown in Table 2.1. The alloy was designed to carry out a basic research on the flow behaviour of matrix phase of normal IN718 alloy, to enhance the understating about the deformation mechanisms. For alloy design, the amount of solid solution strengtheners such as Fe and Cr was increased and precipitate formers like Al, Nb and Ti were reduced along with keeping the carbon content low. With the aforementioned changes in the chemical composition, an IN718WP disc of diameter 195 mm was produced by powder metallurgy route at Voestalpine BÖHLER Edelstahl GmbH (Kapfenberg, Austria). For initial microstructure, SEM

characterization has been performed in the backscattered electron diffraction mode that shows an extremely low amount of precipitates with some pores (see Figure 2.1). The compression tests were conducted employing the Gleeble 3800 simulator at temperatures 900 ^{o}C, 925 ^{o}C, 950 ^{o}C, 975 ^{o}C, 1000 ^{o}C and 1025 ^{o}C and strain rates of 0.01 s^{-1}, 0.1 s^{-1}, 1 s^{-1} and 10 s^{-1}. The hot compression samples were 15 mm long and 8 mm in diameter. We used a K- type thermocouple welded at the sample's surface to control the temperature. More details about the alloy can be found in the work by [96].

Table 2.1. Chemical composition of IN718WP alloy

Elements (wt. %)										
Ni	Cr	Fe	Mo	Al	Co	Si	Nb	C	Mn	Ti
50.18	23	22.07	3.71	< 0.28	0.22	0.1	< 0.28	<0.03	0.1	< 0.03

The hot-deformed and the as-received samples were examined using the EBSD technique. Before the microstructure examination, the samples were hot-mounted, ground with SiC paper, and polished with colloidal silica suspension (OP-S). For EBSD characterization, a TESCAN Mira3 scanning electron microscope was used, along with a Hikari detector. Measurements were conducted with a step size of 0.1 μm for the area of 120 μm × 120 μm. The EBSD data were analyzed using TSL-OIM Analysis v.8, and the Grain orientation spread (GOS), Inverse pole figure (IPF), Kernel average misorientation (KAM) and ODF (Orientation distribution function) maps were obtained. ODF maps consider the Gaussian half-width of 5^{o} and harmonic series expansion method to study the texture evolution properly. The density of dislocations that have been forested during the deformation and, are associated with small misorientations was measured from the EBSD data. It has to be mentioned that, the density of individual dislocations inside the grains can’t be measured through normal EBSD and needs HR-EBSD. Since the substructure size

in this case is in the range of micrometers, our step size for scanning shall capture nearly 10 pixels, which is reasonable to estimate the dislocations in the forested areas. The model for the estimation of dislocation density is adopted from literature [97-99]. The aggregate ρ_b is estimated through the following expression, $\rho_b = \sum \frac{\theta_j f_j}{2b} Z_{mean}$, where, θ_j is the misorientation angle, f_j is the fraction of boundary j, Z_{mean} is the ratio of surface area to volume and b is the Burgers vector equal to 2.54×10^{-10} m.

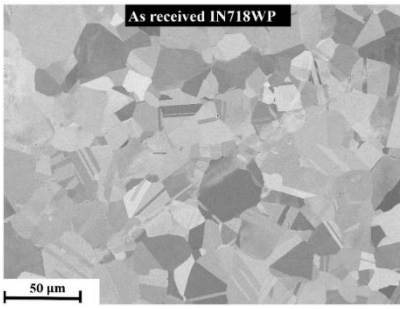

Figure 2.1. BSE image showing the microstructure of the as-received IN718WP

2.3. Model Formulation

As discussed earlier, modelling the flow response relies on governing mechanisms of deformation. IN718WP, being a LSFE material, SH, DRV, and DDRX are expected to occur during hot deformation. Another important aspect is to define internal variables that are microstructure-dependent.

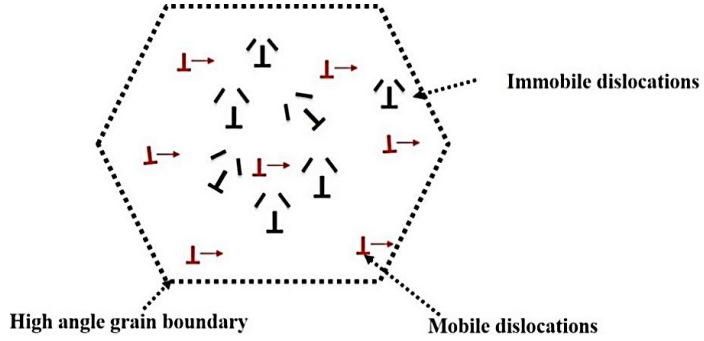

Figure 2.2. Schematic of the assumed microstructure of IN718WP superalloy

Figure 2.2 illustrates the microstructure conceptualization of the IN718WP superalloy in the received condition. This microstructure comprises high-angle grain boundary (HAGB) and mobile and immobile dislocations. In light of this, subsequent sub-sections discuss the model development work.

2.3.1. Constitutive equations

Microstructure provides resistance during deformation in terms of thermal and athermal stresses. Athermal stresses are caused by long-range strengthening contributors: grain boundaries and dislocations. In contrast, thermal stresses contribute to strengthening due to interaction among orthogonal dislocations and strengthening due to the solid solutions. The expression for the flow stress response of deformed alloy can be given as the summation of athermal and thermal stresses and is expressed as [5, 91],

$$\sigma_{deform} = \underbrace{\sigma_{dis} + \sigma_{HP}}_{athermal\ stress} + \underbrace{\sigma_{ss} + \sigma_{gen}}_{thermal\ stress}, \tag{2.1}$$

where σ_{dis} is the strength contribution due to dislocations, σ_{HP} is the strength contribution due to grain size, σ_{ss} is the strength contribution due to solid solutions and σ_{gen} represents the strength contribution due to interaction among orthogonal dislocations. It has to be mentioned that, the first term of Equation (1) σ_{dis} represents the strength contributions due to the parallel interactions of (mobile-mobile and mobile-forest) dislocations and its derivation doesn't consider orthogonal interactions.

The estimation of σ_{dis} is done according to Equation (2.2) and adopted from the Taylor hardening approach as [41, 78, 91, 100],

$$\sigma_{dis} = \alpha M G_T b(\rho_m + w_i \rho_i)^{\frac{1}{2}}. \tag{2.2}$$

In Equation (2.2), α parameter is the dislocation interaction constant related to the dislocation strengthening efficiency, M is the Taylor factor, G_T is the temperature dependent shear modulus, b is the Burgers vector and w_i is the weight parameter used for differentiating the response of the stress fields of the mobile and immobile dislocations under a single dislocation interaction parameter. Furthermore, the Hall-Petch relation delineates the effect of grain size on the strengthening and a more realistic Hall-Petch equation was incorporated from [101], that also considers the influence of strain rate and temperature on strengthening as,

$$\sigma_{HP} = K_{HP}\left(g_{avg}\right)^{-\frac{1}{2}}, \tag{2.3}$$

where $K_{HP} = H_g K_{HP0}\left(\dot{\varepsilon}\left(exp\left(\frac{Q_g}{RT}\right)\right)\right)^{m_g}$ is Hall-Petch parameter that is temperature and strain rate dependent. The concept of strain rate and temperature dependent K_{HP} was taken from [101]. This can be understood in a way that, as the deformation rate and temperature also influence the dislocation mobility, the conventional K_{HP} constant needs to be upgraded to take care of this precisely. At high strain rates, the time for dislocations to arrive at grain boundary is less, thus, the strengthening can be more profound and potentially increasing the K_{HP}. In contrast, at lower strain rates, dislocations have more time to reach at grain boundaries, leading to relatively weaker strengthening, potentially decreasing K_{HP}. It is also known that, at elevated temperature thermal softening affects the strength of grain boundary and it becomes less effective for impeding the dislocations, reflecting a low K_{HP}. At low temperatures, dislocation motion is more restricted, and grain boundaries are more stable thus, strengthening becomes more pronounced, increasing K_{HP}. g_{avg} is the average grain size. K_{HP0} is a pre-factor of Hall-Petch parameter, H_g and m_g are the

materials constant, $\dot{\varepsilon}$ is the strain rate, Q_g is the activation energy, R is the gas constant and T is the temperature.

As one part of alloy strength comes from the solid solution strengthening, its contribution to the flow stress is adopted from the work by [5], as,

$$\sigma_{ss} = \left(\sum_i \sigma_{ss,i}^{3/2} \right)^{2/3}, \tag{2.4}$$

where $\sigma_{ss,i}$ is the solid solution strengthening contribution from i^{th} solute (where i varies from 1 to 7 being, 1:Cr, 2:Nb, 3:Al, 4:Ti, 5:Mo, 6:Fe and 7 for Mn) in the material and expressed as [102, 103],

$$\sigma_{ss,i} = \sigma_{SS,0} \, exp\left(-\frac{1}{C_1} \frac{k_B T}{H_{sol}} ln\left(\frac{\dot{\varepsilon}_{ss}}{\dot{\varepsilon}} \right) \right). \tag{2.5}$$

Herein, $\sigma_{SS,0}$ is zero temperature yield stress, C_1 is a calibration parameter, k_B is the Boltzmann's constant, H_{sol} is the energy barriers to dislocation motion and $\dot{\varepsilon}_{ss}$ is the reference strain rate (see Table 2.3). The pre-factor $\sigma_{SS,0}$ for different solutes can be expressed as [104],

$$\sigma_{SS,0} = A_l M G_T \left(\frac{1}{4\pi^2 N_{cell}} \right)^{4/3} \left(\frac{w}{b} \right)^{1/3} (\epsilon_{mis})^{4/3} \, (X_i)^{2/3}, \tag{2.6}$$

where, A_l is a constant (A_l=$2^{-1/2}$), N_{cell} is the the number of atoms in the unit cell (N_{cell}=*4*), w is the range of action of a diffuse obstacle (w/b = 1.7) [104], and X_i is the mole fraction of i^{th} alloying element, where i varies from 1 to 7, being 1:Cr, 2:Nb, 3:Al, 4:Ti, 5:Mo, 6:Fe and 7 for Mn. In Equation (6), ϵ_{mis} is the total misfit, that includes size misfit (δi) and modulus misfit ($\eta i'$) of i^{th} alloying element, where i varies from 1 to 7, being 1:Cr, 2:Nb, 3:Al, 4:Ti, 5:Mo, 6:Fe and 7 for Mn, adapted from [5, 105] as,

$$\epsilon_{mis} = \alpha_{mis}\delta_i + \eta_i', \tag{2.7}$$

where α_{mis} is a factor considered to be 16 and $\eta_i' = \eta_i(1 + |\eta_i|/2)$. η_i is adopted from [5] for the individual elements for the calculation. In Equation (2.5), the energy barrier H_{sol} is calculated as,

$$H_{sol} = 5.5 \cdot G_T \cdot b^3 \cdot \left(\frac{w}{b}\right)^{\frac{1}{3}} \cdot \left(\frac{\sigma_{SS,0}}{MG_T}\right)^{\frac{1}{2}}. \tag{2.8}$$

Another short-range contributor that participates in flow stress arises due to interaction between orthogonal dislocations, which is described as [34, 106],

$$\sigma_{gen} = S_{dis}G_T\left[1-\left(\frac{k_BT}{A_{dis}G_Tb^3}ln\left(\frac{\dot{\varepsilon}_{rf}}{\dot{\varepsilon}}\right)\right)^{1/q}\right]^{1/p}, \tag{2.9}$$

where S_{dis} and A_{dis} are calibration parameters and $\dot{\varepsilon}_{rf}$ is a constant (see Table 2.3). The exponents $0 < p < 1$ and $1 \leq q \leq 2$ are related to the shape of the energy barrier and given in Table 2.4.

2.3.2. Microstructural rate equations

In case of LSFE materials, SH, DRV and DDRX phenomena cause the microstructure change during deformation. The plastic strain accumulates during the hot deformation and increases the stored energy. The operation of the Frank-Read sources will produce more mobile dislocations. This newly produced dislocations will travel and after encountering an obstacle, i.e., substructure boundary, it gets immobilized. Dislocation annihilation occurs due to dislocation climb and glide movements. Therefore, the rate of mobile dislocation density with respect to strain can be given as [47, 58, 78],

$$\frac{d\rho_m}{d\varepsilon} = \frac{M}{b}\left[\underbrace{\frac{1}{\lambda_{mean}}}_{F-R\ source} - \underbrace{\frac{1}{s}}_{immobilization} - \underbrace{\frac{8\rho_m^{\frac{1}{2}} v_{cl}}{v_{gl}}}_{climb\ recovry} - \underbrace{d_{DRV}(\rho_m + \rho_i)}_{glide\ recovery}\right], \tag{2.10}$$

where, λ_{mean} is mean free path for glide and d_{DRV} is the glide recovery annihilation distance. Higher the d_{DRV} value, faster the dynamic recovery. s is dislocation substructure size and estimated as,

$$s = \frac{k_c}{(\rho_i)^{1/2}} \tag{2.11}$$

where k_c is a parameter related to the substructure formation by dislocations and expressed as (Moretti et al., 2023),

$$k_c = \frac{12 \cdot \pi \cdot C_\alpha \cdot (1 - \vartheta)}{(2 + \vartheta)} \tag{2.12}$$

where C_α is constant and ϑ is the Poisson's ratio. The mobile dislocations glide and get annihilated with other mobile dislocations or immobile dislocations, if the interaction is within the distance d_{DRV}. Temperature and strain rate dependent d_{DRV} can be given as [29],

$$d_{DRV} = A_v g^{m_v} (\dot{\varepsilon})^{-n_v} e^{\left(-\frac{Q_v}{RT}\right)^{n_v}}, \tag{2.13}$$

where g is the initial grain size, A_v, m_v, Q_v *and* n_v are materials constant and R is the gas constant. The immobilization of the dislocations increases the density of immobile dislocations. At the same time, its density reduction may occur due to climb and glide annihilation. Inconel 718WP is an LSFE material, and hardening dominates over recovery. Thus, the dislocation density and the stored energy within the grains increase. The DDRX phenomenon starts at the grain boundaries to vent out the stored energy by nucleating regions with low dislocation density. These regions then

apply pressure to the high-angle grain boundary, large enough to move it. The evolution of immobile dislocation density with respect to strain is formulated as [47, 58, 78],

$$\frac{d\rho_i}{d\varepsilon} = \frac{M}{b}\left[\underbrace{\frac{1}{s}}_{Immobilization} - \underbrace{8\frac{v_{cl}}{\lambda_{mean}}\rho_i\left(\frac{1}{\rho_m v_{gl}}\right)}_{climb\ recovery} - \underbrace{d_{DRV}\rho_i}_{glide\ recovery}\right] - \underbrace{\frac{d\rho_{DDRX}}{d\varepsilon}}_{DDRX}, \tag{2.14}$$

where $(d\rho_{DDRX})/d\varepsilon$ is the reduction rate of dislocation density due to DDRX phenomena.

The glide velocity of dislocation under the action of external stress is influenced by the thermal and athermal barriers. Thermally activated overcoming of obstacles results in a jerky motion in the crystal and characterized by variations in dislocation velocity as [107, 108],

$$v_{gl} = \lambda_{mean} v_0 exp\left(-\frac{\Delta G}{k_B T}\right) sign(\sigma_{SR_{eff}}) \tag{2.15}$$

In Equation (2.15), v_0 is attempt frequency, ΔG is the average activation energy needed to overcome the obstacles, and $\sigma_{SR_{eff}}$ is the difference between the total flow stress and athermal stress as [78],

$$\sigma_{SR_{eff}} = \sigma_{deform} - \sigma_{dis} - \sigma_{HP} \tag{2.16}$$

The climb velocity of the dislocation is very much dependent on the migration of vacancies and atom to/or from the dislocation core, providing the possibilities to move it perpendicular to the slip plane. The process of climbing can be regulated by core diffusion and is linked to a certain activation energy [109] . The climb velocity models have been proposed in the literature by different researchers[110, 111] . In this work, v_{cl} was adopted from [47, 57, 112], as

$$v_{cl} = \frac{2\pi\eta\Omega D_s \sigma_{cl}}{bk_B T\left(1-\eta ln\left(\frac{L_{climb}}{\lambda_{dis}}\right)\right)}, \tag{2.17}$$

Herein, η is Coefficient for transfer of defects into jogs, Ω is the atomic volume, D_s is the self-diffusion coefficient and λ_{dis} is average dislocation distance for climb. In Equation (2.17), L_{climb} is the length associated with elastic interactions between dislocations and defects and expressed as,

$$L_{climb} = \frac{1}{6\pi}\left(\frac{1+\vartheta}{1-\vartheta}\right)\frac{G_T \Omega}{k_B T} \tag{2.18}$$

Average dislocation distance for climb can be estimated by considering the Pythagorean summation and taking all dislocations as [113, 114],

$$\frac{C_k}{\lambda_{dis}} = \frac{1}{h_m} + \frac{1}{s} \tag{2.19}$$

Herein, C_k is the constant that is related to number of dislocations passed by the obstacles and h_m is mobile dislocation spacing. The climb stress σ_{cl} associated with the climb velocity can be estimated as [47, 78],

$$\sigma_{cl} = \frac{G_T b}{2\pi(1-\vartheta)\lambda_{dis}} \tag{2.20}$$

2.3.3. Mean free path of glide

The dislocations glide a distance λ_{mean} before they are annihilated or immobilized at different obstacles. Figure 2.3 depicts the different interaction possibilities when a mobile dislocation glides. It may encounter another mobile dislocation, immobile dislocations or a grain boundary before immobilizing. The mean free path can be estimated by considering the Pythagorean summation and taking all the possibilities as [113, 114],

$$\frac{C_k}{\lambda_{mean}} = \frac{1}{h_m} + \frac{1}{s} + \frac{1}{g_{avg}} \tag{2.21}$$

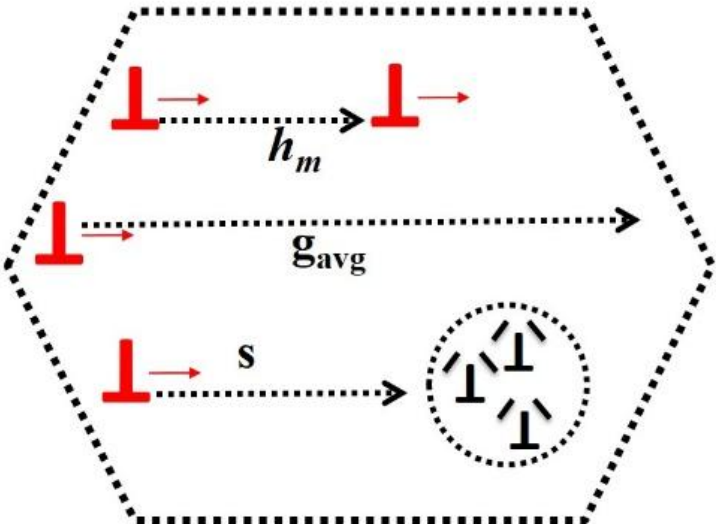

Figure 2.3. Schematic diagram depicting the different possibilities of dislocation interactions that enable estimating the mean free path

2.3.4. Discontinuous dynamic recrystallization (DDRX)

The flow stresses are governed by the dominating mechanism among work hardening and softening due to dynamic recovery and DDRX. The DDRX phenomenon requires to achieve a critical dislocation density (ρ_c) for its manifestation. This criterion is met when the immobilization of dislocations leads to increase in the dislocation density across the grain boundaries and corresponding stored energy. Figure 2.4 shows schematically the evolution of the microstructure of IN718WP superalloy, (a) as-received and (b-d) deformed states. When the dislocation density during the deformation reaches a critical value, DDRX triggers and new grains nucleate. Grain boundary bulging occurs across the pre-existing interfaces, and thus, new dynamic recrystallized grain forms. The equation of the critical dislocation density for dynamic recrystallization during hot deformation was originally proposed by [115]. Many researchers further explored and modified it to address the DDRX phenomenon [29, 64, 116-119]. In this work ρ_c was adopted

from [29], as given in equation (2.22). The detailed mathematical derivation for ρ_c is discussed in the literature [117] .

$$\rho_c = \left(\frac{20\gamma_{gb}\dot{\varepsilon}}{3b\lambda_{mean}M_{gb}\tau^2}\right)^{1/3}, \tag{2.22}$$

In Equation (2.22), $\gamma_{gb} = \left(\frac{G_T b\theta_m}{4\pi(1-\vartheta)}\right)$ is the grain boundary energy per unit area and $M_{gb} = \frac{b\delta D_{ob}}{k_B T} exp\left(-\frac{Q_{gb}}{RT}\right)$ is the mobility of the grain boundary and $\tau = G_T b^2/2$ is the dislocation line energy. θ_m is the misorientation angle for HAGBs adopted to be 15 degree [29, 118], δ is grain boundary thickness, D_{ob} is grain boundary diffusion coefficient and Q_{gb} is grain boundary diffusion activation energy.

Once the DDRX phenomenon triggers, its fraction (X_{DDRX}) can be estimated as per Equation (2.23) [73]. The detailed derivation for the X_{DDRX} is described in Appendix 2.A.

$$X_{DDRX} = \left(1 - exp(-qNv^3t^4)\right), \tag{2.23}$$

where $q = 4\pi/3$ is a shape factor, N is the number of DDRX nuclei, $v = M_{gb}P$ is the velocity of the grain boundary, P is the pressure on the grain boundary and t is the time. The nucleation rate per unit grain boundary area for DDRX is calculated by Equation (2.24) [73, 118].

$$\frac{dN}{d\varepsilon} = C_{DDRX}\dot{\varepsilon} exp\left(-\frac{Q_n}{RT}\right), \tag{2.24}$$

where C_{DDRX} and Q_n represent the DDRX coefficient and activation energy, respectively, for the nucleation. During hot deformation, the original grains continuously evolve across the microstructure under varying deformation conditions. Thus, the average grain size can be estimated according to the rule of mixture in Equation (2.25),

$$g_{avg} = X_{DDRX}\, g_{drx} \quad + (1 - X_{DDRX}) g, \tag{2.25}$$

where the g_{drx} is the dynamic recrystallized grain size. Herein, g_{drx} is considered to be extensively influenced by coarsening and nucleation of DDRX grain and adopted from the work by He et al. [101] and Lin et al.[29] as,

$$g_{drx} = \overbrace{A_r g^{m_r} \left(\dot{\varepsilon} exp\left(\frac{Q_r}{RT}\right)\right)^{n_r}}^{\text{coarsening}} - \overbrace{a_2 (X_{DDRX})^{a_3}\, g^{a_4}}^{\text{shrinkage due to nucleation}} , \tag{2.26}$$

where A_r, m_r, n_r, Q_r, a_2, a_3 and a_4 are the material parameters. The first term on right hand side of Equation (2.26) represents the increase in grain size due to coarsening and second term represents the shrinkage due to nucleation. Since the DDRX process is complex, researchers have developed the Equation (2.26), based on many observations. The material parameters represent that these processes of nucleation and growth during hot deformation conditions are not linear. Thus, based on experimental observations these parameters and constants are extracted and remains constant with temperature, and strain rate making it useful for a wide range processing conditions. The consumption rate of dislocations with respect to strain in the DDRX region is adopted from the research work of [29, 64] and estimated by Equation (2.27) as,

$$\frac{d\rho_{DDRX}}{d\varepsilon} = (\rho_{imob} - \rho_c) X_{DDRX} F_{drx} \dot{\varepsilon}, \tag{2.27}$$

where F_{drx} is dynamic recrystallization coefficient that represents the rate of dynamic recrystallization during the DRX phenomena. The higher the F_{drx} value, the faster recrystallization will occur leading to faster nucleation and growth of DRX grain, see Appendix 2.A.

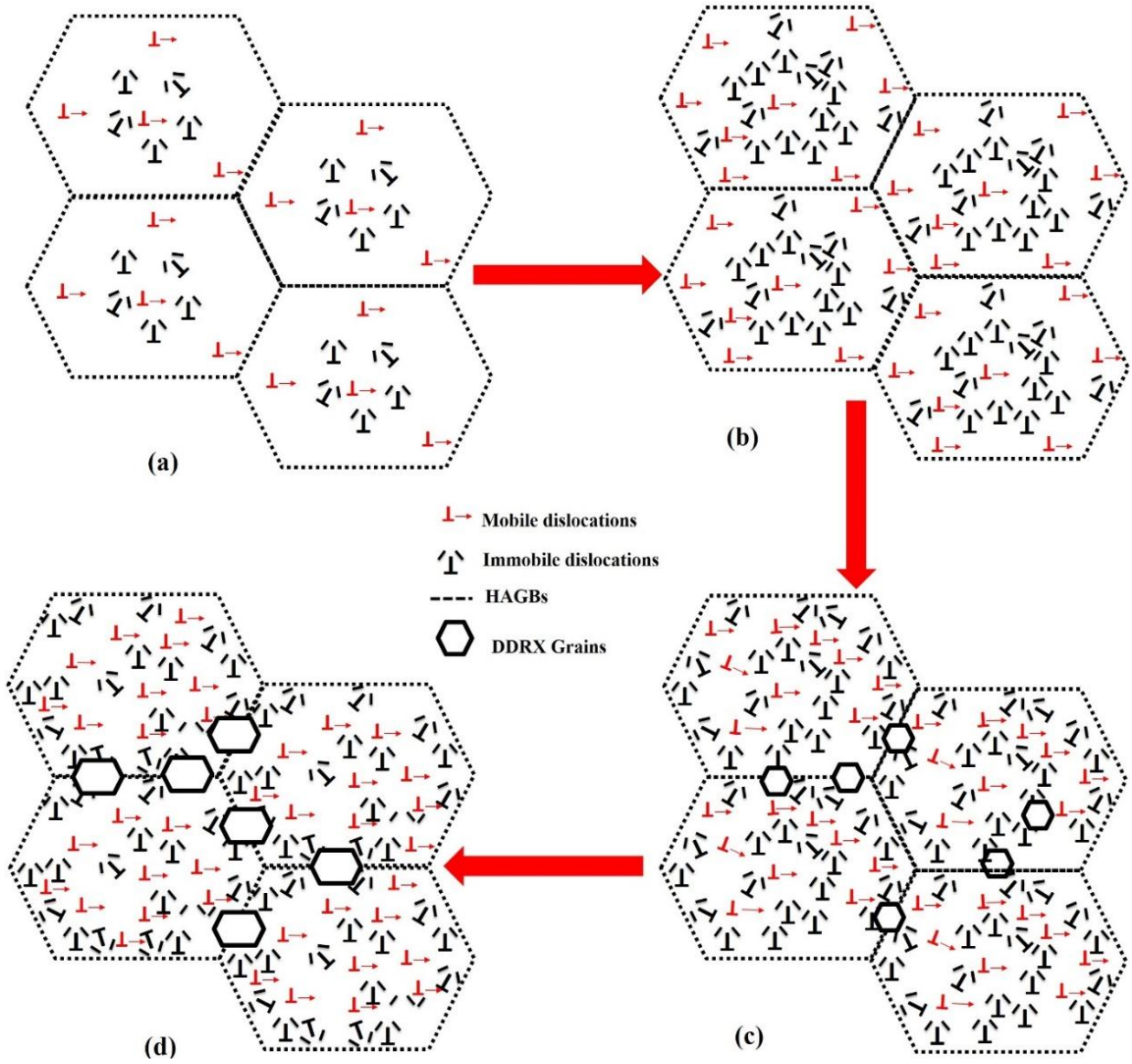

Figure 2.4. Illustration of the microstructure in IN718WP; (a) as-received condition, (b) before reaching the ρ_c for DDRX, (c) reaching ρ_c (d) after reaching ρ_c during deformation.

The flow stress in the DDRX region is calculated according to Equation (2.28) and adopted from the research work by [116] for AISI 202 austenitic stainless steel.

$$\sigma_{DDRX} = \alpha M G_T b (\rho_{DDRX})^{1/2} \tag{2.28}$$

The total flow stress response during the hot deformation can be estimated using the rule of the mixture of non-recrystallized and recrystallized area-averaged over the polycrystal as [116, 120] ,

$$\sigma_{total,flow} = (1 - X_{DDRX})\sigma_{deform} + X_{DDRX}\sigma_{DDRX} \quad (2.29)$$

It has to be mentioned that, the model relies on mean values of the initial input parameters, such as dislocation densities and grain size, that need to be fed to the model. Also, it is assumed that deformation is homogenous, and the model doesn't consider any flow localization and geometrical instabilities. The model has used simplified equations that offers an effective balance between physical representation and computational ease.

2.4. Solution for constitutive equations and optimization of parameters

The specified constitutive Equations (2.1–2.29) were solved using MATLAB software and the ODE (Ordinary Differential Equations) - 45 solver. The Runge-Kutta method is the basis for the working of ODE-45 solver, and at each step of deformation, the solution is obtained and saved. Additionally, the ODE 45 solver uses the fifth-order Runge-Kutta method, adding to the numerical computation with accurate results. Herein, the model operates on the average values of the variables that remain constant throughout the microstructure. The initial mobile and immobile dislocation densities and grain size are the physical inputs used by the model shown in Table 2.2. Initial dislocation density has been taken from a similar type of alloy IN718. The alloy reported by Pradeep et al. [121] was the parent alloy and authors considered as a good starting point. Amount of dislocations are highly dependent on the chemical composition and heat treatments, but huge experimental challenges always lie in measuring the density of different dislocation configurations. It has been reported that the combination of XRD and TEM supplemented by HR-EBSD may only provide accurate density of different dislocation configurations. Other way to deal this problem is to take data from literature, from parent alloy/similar alloy.

Table 2.2. Microstructure-based parameters as input for this work

Microstructure based inputs	Magnitude	Reference
Initial mobile dislocation density, ρ_{m0} Eq.(2.10)	$08.15 \times 10^{12.0}$ m^{-2}	[121]
Initial immobile dislocation density, ρ_{i0} Eq.(2.14)	$01.78 \times 10^{13.0}$ m^{-2}	[30, 121]
Initial grain size, g Eqs.(2.13, 2.26) and Appendix Eq.(2.A.5)	$20.00 \times 10^{-6.0}$ m	Experiment

Parameters were optimized by minimizing the discrepancies or relative errors between the simulated flow stress produced by the model and the experimental data. Relative errors arise from factors such as the nature, quantity, and quality of the experimental data, model's description and accuracy, and the chosen calibration parameters. Optimization algorithms were employed to adjust the fitting parameters, ensuring the simulated results align as closely as possible with the experimental values. The objective function is minimized using optimization algorithms, implemented in MATLAB. The process begins with problem configuration, where a function is defined to establish the initial conditions and structure of the problem. This involves in putting boundary conditions (temperature, strain rate, and strain), the initial microstructure, constant parameters, and an initial guess for the fitting parameters into the model. The model then uses these inputs to estimate the flow stress and microstructural based variable. The simulated outputs are subsequently compared with the corresponding experimental data to evaluate the objective function. If the objective function value is below the specified tolerance, the current parameters are deemed optimized, and the process concludes. Otherwise, the function value is fed back to the optimizer, which uses this feedback to generate a new set of parameters as input to the model. This iterative process continues until the optimization achieves the desired convergence or meets

predefined termination criteria. For this Nelder-Mead simplex algorithm, as done in the work by [122] was utilized. To initiate the optimization, the initial guess values of each parameter was required and collected from the literature. In this approach, n-dimensional vectors *a* were represented by a simplex of *p + 1* points. Before employing these *n* vectors as simplex components in addition to a_0, the algorithm first creates a simplex around the original guess a_0 by adding 5% of each component $a_0(i)$ to a_0. Since the parameters in our framework are confined to bounded intervals, the standard fminsearch function is not directly applicable. To overcome this limitation, we employed the modified function fminsearchbnd [123], which supports constrained variables and was adapted for our specific needs in this study. Herein, an objective function was calculated according to Equation (2.30) based on the Nelder-Mead simplex method [122] that minimizes the error between experimental and simulated results.

$$Objective\ function = \sqrt{\frac{(Experimental\ flow\ stress - Simulated\ flow\ stress)}{Experimental\ flow\ stress}} \qquad (2.30)$$

Single set of parameters were obtained from 12 experimental curves only, i.e., (0.01 s^{-1}, 0.1 s^{-1}, 1s^{-1} and 10 s^{-1}) at 1000 ^{o}C, 925 ^{o}C and 950 ^{o}C. Rest of the 11 curves were predicted by the model using those parameters. The approach used in the present chapter is helpful to reduce the experiments and can predict multiple flow curves along with the corresponding microstructure evolution. The model predictions are validated with respect to flow curves, DDRX fraction and dislocation density for the soundness of model. This work also verified the model's accuracy during plastic deformation under both moderate and large strain rate and temperature conditions, respectively. Figure 2.5 shows schematic illustration of the mean-field approach proposed in this work. The materials constants and calibrated parameters incorporated in the model are also delineated in Table 2.3 and Table 2.4.

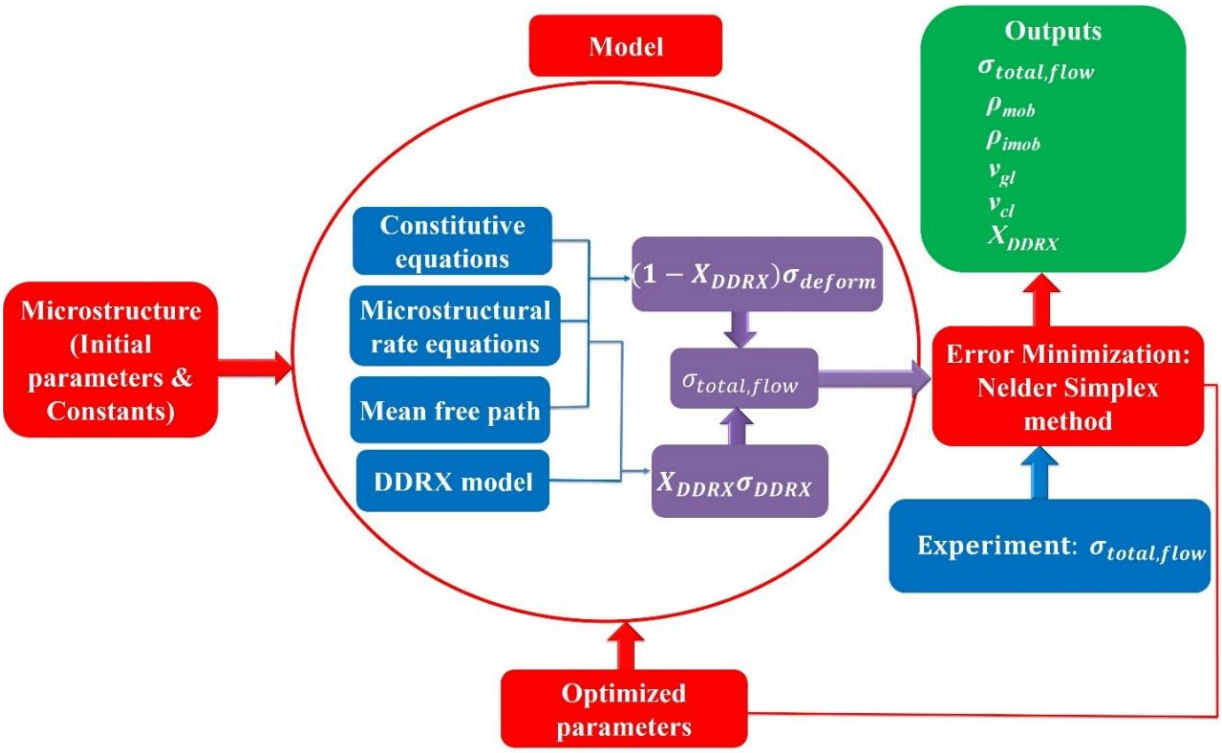

Figure 2.5. Schematic illustration of the mean-field model proposed in this work.

Table 2.3. Material constants used in the model

Parameter	**Equations**	**Magnitude**	**Reference**
b (m)	(2.2,2.10, 2.14, 2.17, 2.20, 2.22, 2.28)	$2.54 \times 10^{-10.0}$	[64]
G_T *(Pa)*	(2.2, 2.6, 2.8,2.9, 2.18, 2.20, 2.28)	$(-0.0323\times(T-273) + 80.1112) \times 10^{9.0}$	[124]
k_B *(J/k)*	(2.5, 2.9, 2.15, 2.17,2.18)	$1.3806504\times 10^{-23.0}$	-
R(J/mol/k)	(2.13, 2.24, 2.26)	8.314	-
ϑ	(2.12,2.18)	0.31	[64]
M	(2.2, 2.6, 2.8, 2.10,2.14, 2.28)	3.06	[41]
$\dot{\varepsilon}_{ref}$	(2.9)	3.06×10^{6}	[5]
$\dot{\varepsilon}_{ss}$	(2.5)	1×10^{5}	[5]
$\sigma_{SS,0}$	(2.5)	~108 MPa	[125]

Table 2.4. Optimized parameters used in the model

C_k	α	C_{DDRX}	v_0, HZ	Q_{gb} (KJ/mole)	A_x
Eqs.(2.19,2.21)	Eqs.(2.2, 2.28)	Eq.(2.24)	Eq.(2.15)	Eq.(2.22)	Eq.(2.A.5)
12.98	0.2	~$4.47\times 10^{28.0}$	$2\times 10^{13.0}$	68.24	3306.65
p	q	A_v	Q_x (KJ/mole)	Q_s (KJ/mole)	m_x
Eq.(2.9)	Eq.(2.9)	Eq.(2.13)	Eq.(2.A.5)	Eq.(2.A.4)	Eq.(2.A.5)
0.60	0.43	$2.04\times 10^{-13.0}$	791.36	287.43	-0.269
η	S_{dis}	a_3	Q_n (KJ/mole)	$\Delta G, J$	A_{dis}
Eq.(2.17)	Eq.(2.9)	Eq.(2.26)	Eq.(2.24)	Eq.(2.15)	Eq.(2.9)
0.005	0.004	0.66	707.11	$4.50\times 10^{-19.0}$	0.68
A_r	n_r	$Q_v, KJ/mole$	$\delta D_{ob}(m^3/s)$	K_{HP0}, MPam$^{0.5}$	m_r
Eq.(2.26)	Eq.(2.26)	Eq.(2.13)	Eq.(2.22)	Eq.(2.3)	Eq.(2.26)
0.05	-0.15	440.99	$6.26\times 10^{-15.0}$	$0.35\times 10^{6.0}$	0.29
C_α	C_1	H_g	Q_g (KJ/mole)	m_g	a_2
Eq.(2.12)	Eq.(2.5)	Eq.(2.3)	Eq.(2.3)	Eq.(2.3)	Eq.(2.26)
3.98	2.50	0.27	191.78	0.07	1.54
a_4	m_v	n_v	n_x	Q_r, (KJ/mole)	w_i
Eq.(2.26)	Eq.(2.13)	Eq.(2.13)	Eq.(2.A.5)	Eq.(2.26)	Eq.(2.2)
1.28	-1.27	0.10	-0.06	393.51	0.39

2.5. Results and discussion

2.5.1. Flow curves

Figures 2.6a, b, c, d, e, and f show the comparison of experimental and simulated flow curves of the IN718WP superalloy for the wide range of strain rates and temperatures, 0.01 s^{-1} - 10 s^{-1} and

900 °C - 1025 °C, respectively.

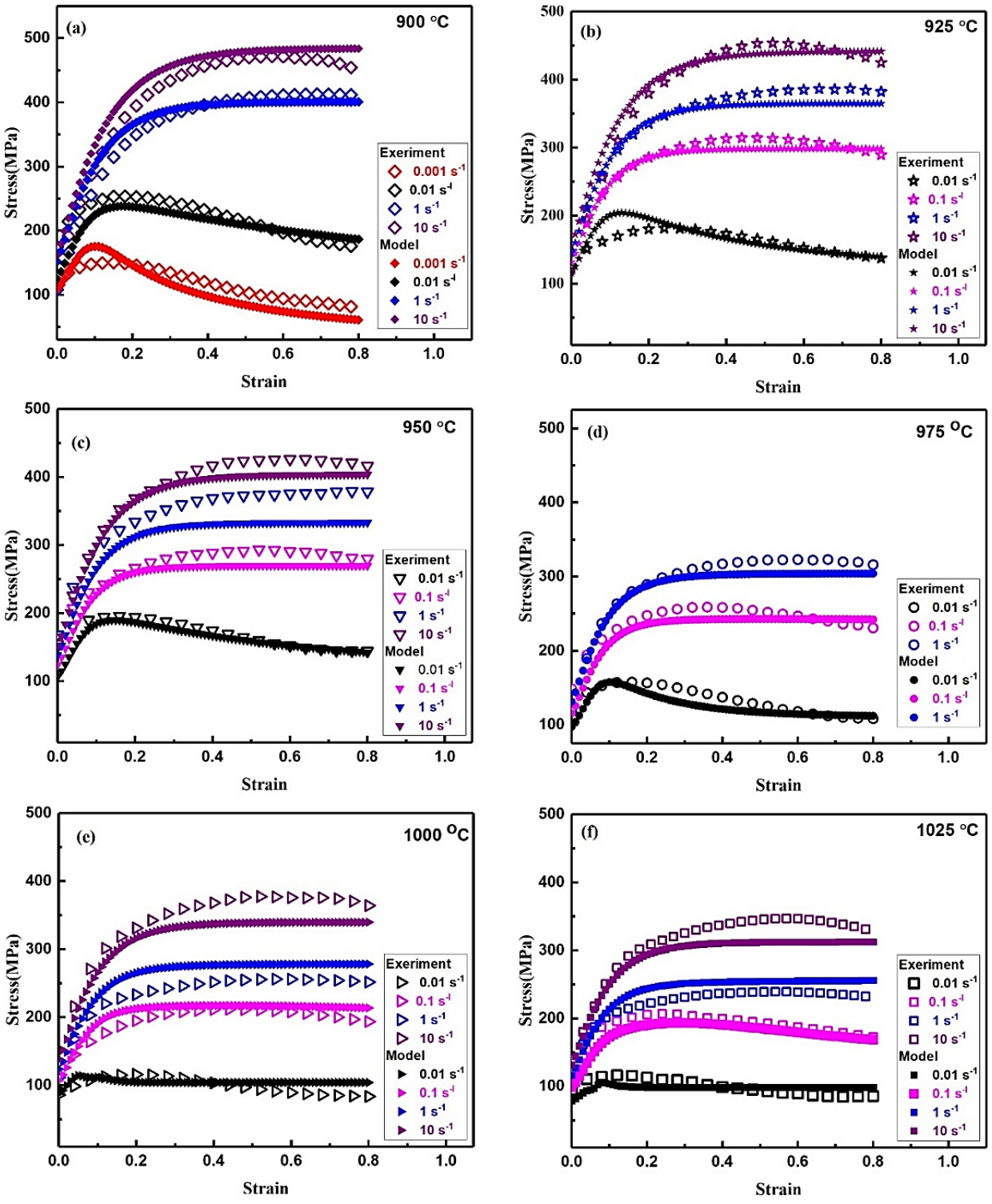

Figure 2.6. Experimental and simulated flow stress curves of IN718WP at different strain rates (0.001 s^{-1}- 10 s^{-1}) and temperature (a) 900 °C, (b) 925 °C, (c) 950 °C, (d) 975 °C, (e) 1000 °C and (f) 1025 °C

The experimental and modelled flow curves showed a good agreement. Similarly, Figure 2.7 shows the modelled and experimental flow curves at varying temperatures for the strain rate 1 s^{-1}. The strain corresponding to peak flow stress (peak strain) varies for different conditions.

At lower temperatures or higher strain rates, the onset of deformation is preceded by SH and DRV, which also results in delayed peak strain (for example see flow curve of 10 s^{-1}/ 950 ^{o}C). At higher temperatures or lower strain rates, the peak strain is preceded by SH and followed by softening due to DRV and DDRX (drop in stress after peak) and further flat region, respectively. These observations are related to a reduced driving force and earlier (in terms of strain) occurrence of the dynamic recrystallization phenomenon at higher temperatures/reduced strain rates [126].

In addition to this, deforming at lower strain rates, there is enough time for the nucleation and growth of DDRX grain, which also reduces the strain at which recrystallization starts [126] (see flow curves of 0.1 and 0.01 s^{-1} / 925 ^{o}C). It has to be mentioned that model do not considers the adiabatic heating, dynamic strain ageing and flow localization due to damage.

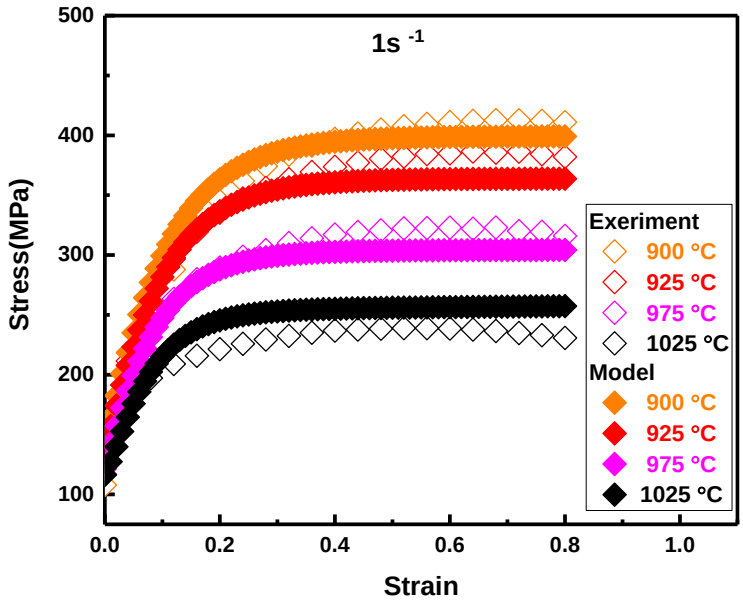

Figure 2.7. Experimental and simulated flow stress curve of IN718WP at 900 ^{o}C - 1025 ^{o}C / 1 s^{-1}

2.5.2. DDRX fraction and average grain size

Figure 2.8 shows the IPF map superimposed with high-angle grain boundaries (HAGBs ~ 15-60 °) and KAM maps for the as-received. IPF map shows the nearly polygonised grains with the presence of twins. The non-homogenous distribution of KAM values (green and blue color variation) indirectly indicated the presence of GNDs and corresponding stored energy across the microstructure [127].

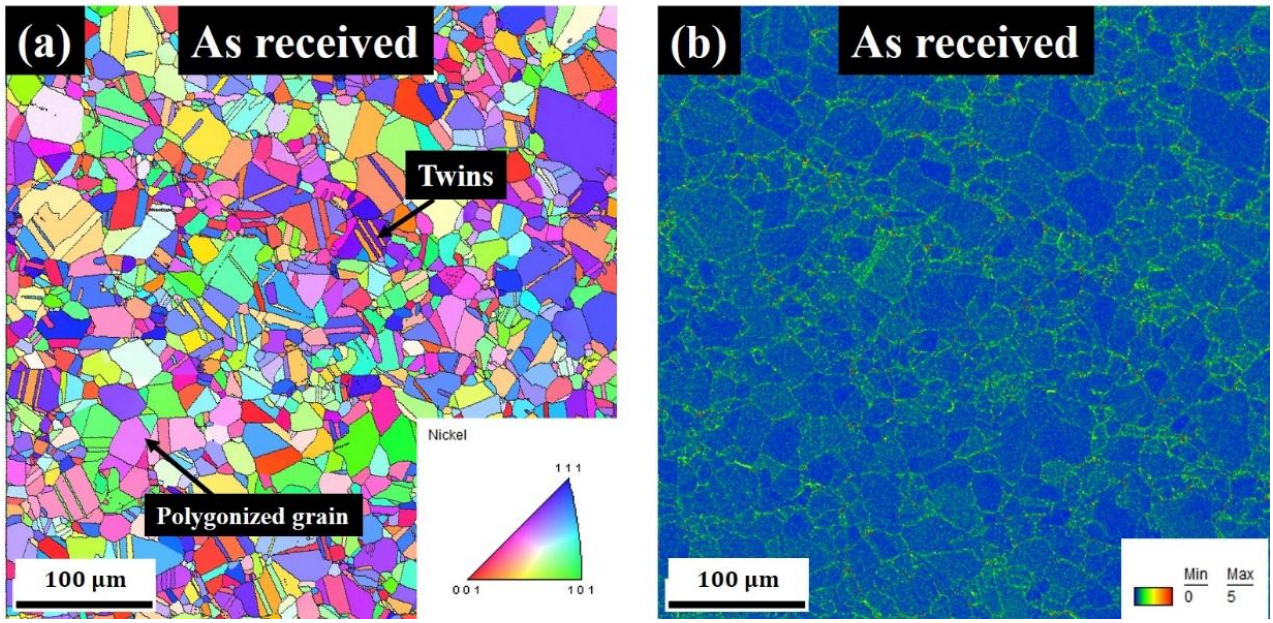

Figure 2.8. As received IN718WP superalloy (a) IPF Map and (b) KAM Map

Figure 2.9 depicts the evolution of the modelled grain size and recrystallized fraction with ongoing deformation at different temperatures and strain rates. The average grain size reduces and approaches a steady state at low strains when deforming at low strain rates or higher temperatures. This indicates that low strain rates or higher temperatures favor the DDRX process because of the extended time available for DDRX nucleation and growth at low strain rates, along with increased

grain boundary mobility at higher temperatures [29, 64, 79, 128]. In contrast, larger average grain size and low fraction of recrystallization are predicted at higher strain rates or lower temperatures.

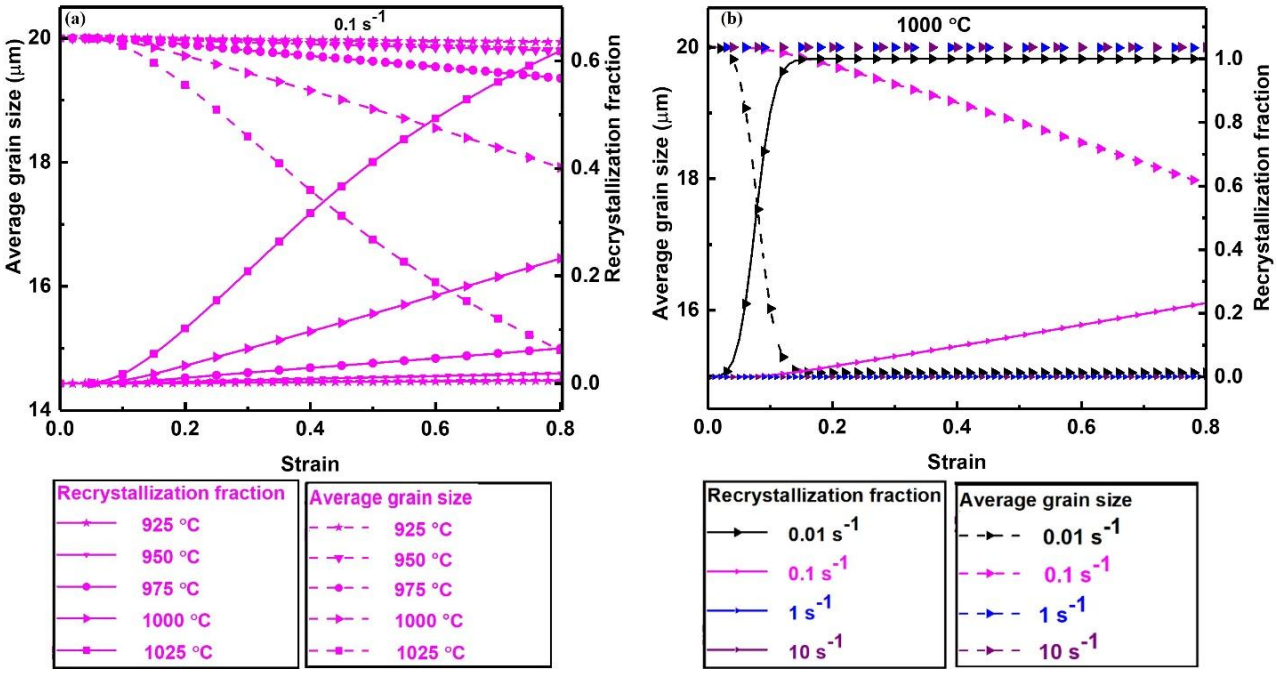

Figure 2.9. Variation of predicted average grain size and recrystallization fraction at (a) 925 °C-1025 °C / 0.1 s^{-1} and (b) 0.01 s^{-1} - 10 s^{-1} / 1000 °C

Figures 2.10a, d and g depict the IPF map superimposed with HAGBs for the samples compressed at 900 °C / 0.001 s^{-1} ,1000 °C / 0.1 s^{-1} and 1000 °C / 0.01 s^{-1}, respectively. Figures 2.10b, e and h depict the KAM maps for same conditions. IPF map shows the elongated grain and deformed annealing twins at 1000 °C / 0.1 s^{-1}. Similarly, at 1000 °C, decreasing the strain rate from 0.1 s^{-1} to 0.01 s^{-1} increases the DDRX fraction and grain size. Corresponding KAM values can be seen to be varying for these conditions, see Figure 2.10e and h. In this work, higher KAM values for 1000 °C / 0.1 s^{-1} in comparison to 1000 °C / 0.01 s^{-1} corresponds to the hybrid microstructure containing DDRX grain as well as accumulation of dislocations that results in more stored energy. Figure

2.10a, b and c depict the fine recrystallized grains at 900 ℃ / 0.001 s^{-1}, however the grain growth was not dominant due to relatively lower temperature. These findings are consistent with the literature reported for Ni-based superalloys [129].

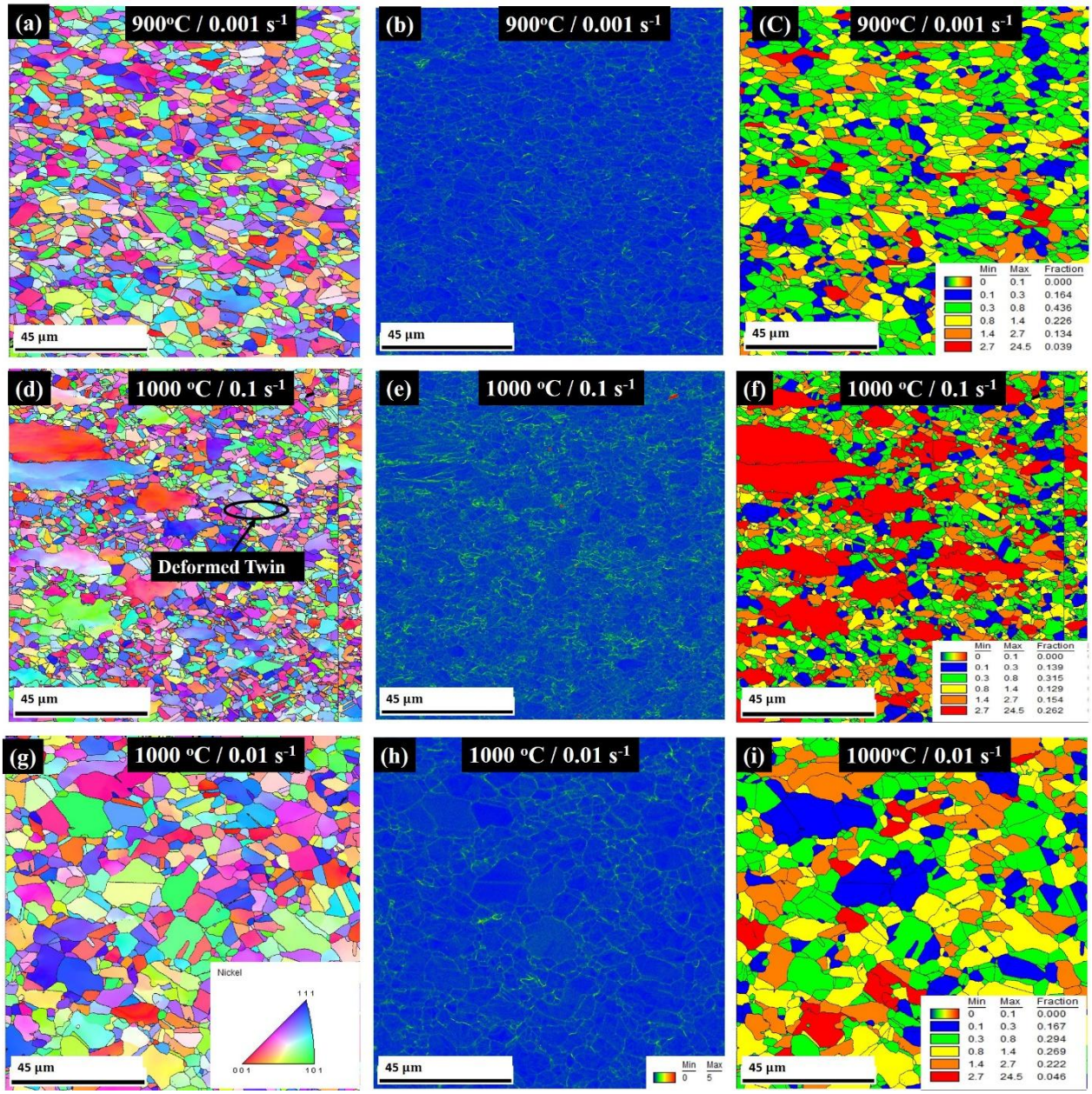

Figure 2.10. Hot compressed IN718WP superalloy: IPF map (a, d and g); KAM map (b, e and h); GOS map (c, f and i) for , 900 ℃ / 0.001 s-1, 1000 ℃ / 0.1 s^{-1} and 1000 ℃ / 0.01 s^{-1}, respectively.

Figures 2.10c, f and i depict the GOS maps for the sample hot compressed at 900℃ / 0.001 s^{-1}, 1000℃ / 0.1 s^{-1} and 1000 ℃ / 0.01 s^{-1}, respectively. GOS map was used for the identification of recrystallized grain. Herein, a GOS value smaller than 2.7 was considered as the visualization of recrystallized grain following literature [96, 130]. In the GOS maps, the blue, yellow and green colors represent mostly recrystallized region. Similarly, the red color in GOS map corresponds to heavily deformed and non-recrystallized grains, respectively. The predicted DDRX grain sizes from the model were 13.11 μm, 11.03, μm and 15.05 μm for 900 ºC /0.001 s^{-1},1000 ºC /0.1 s^{-1} and 1000 ºC /0.01 s^{-1}, respectively. In comparison, the measured DDRX grain sizes were 11.18 ± 1.52 μm, 10.07 ± 1.84 μm and 14.01 ± 2.76 μm under the same conditions.

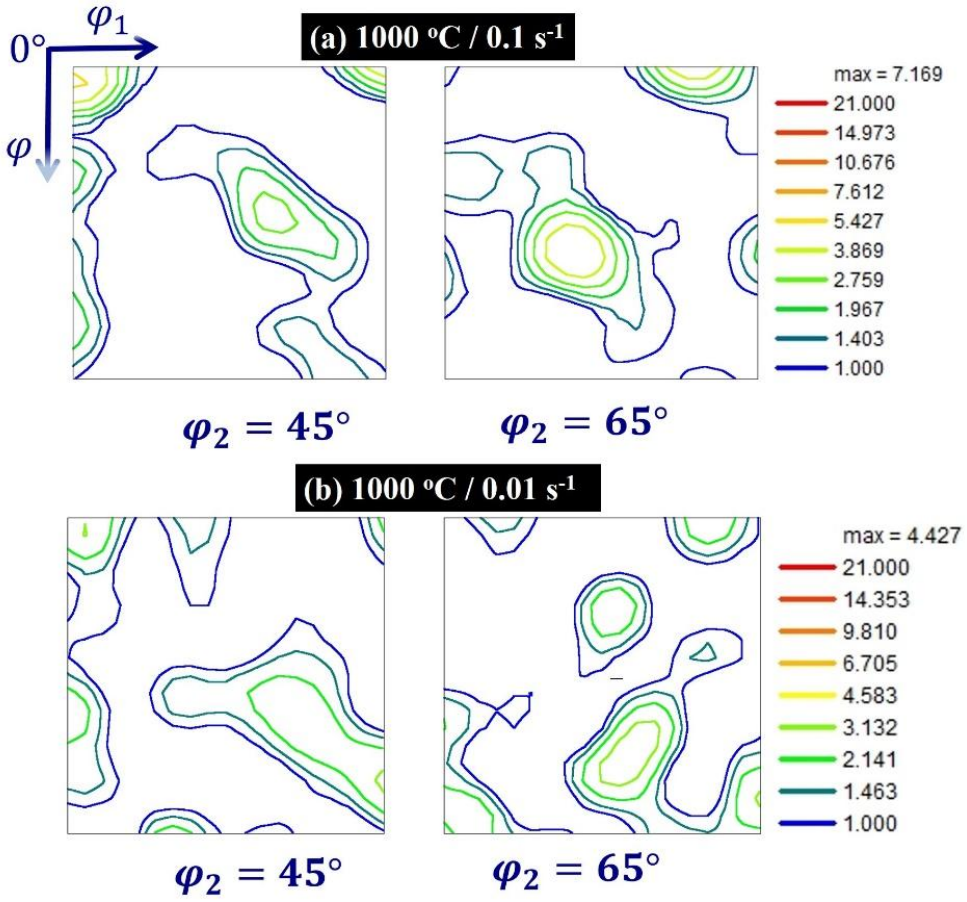

Figure 2.11. (ODF) Map for the section Ø=45° and 65° at 0.8 strain (a)1000 ºC /0.1 s^{-1} and (c)1000 ºC /0.01 s^{-1}

Figures 2.11 a and b depict the Orientation Distribution Function (ODF) maps for $\emptyset_2$ = 45° and 65° for the deformed samples at 1000 ºC /0.1 s^{-1} and 1000 ºC /0.01 s^{-1}, respectively. It can be observed that the sample deformed at 1000 ºC /0.01 s^{-1} shows less texture intensity as compared to 1000 ºC /0.1 s^{-1}. This is due to the more orientation randomization caused by the formation of new DRX grains at 1000 ºC /0.01 s^{-1}. In case of 1000 ºC /0.1 s^{-1} the observed texture components were Shear $(001)\langle 110\rangle$ and Inverse Brass $(112)\langle 110\rangle$. With decrease in strain rate from 0.1 s^{-1} to 0.01 s^{-1} at 1000 ºC, the texture components were Shear $(001)\langle 110\rangle$ and weak Brass $(011)\langle 211\rangle$ and weak Goss $(011)\langle 211\rangle$. Similar texture evolution resulting from the formation of DRX grain during the hot deformation in Nickel based super alloy has been reported in the literature [83, 84]. The model predictions are important in this context in a way that, at 1000 °C, at a strain rate of 0.01 s^{-1} model predicts a higher recrystallization fraction supported by the lower texture intensity. Whereas a strain rate of 0.1 s^{-1} at same temperature predicts a lower recrystallization fraction supported by the presence of higher texture intensity.

Figure 2.12 compares the simulated and experimentally calculated recrystallization fraction for IN718WP using GOS map at 1000 ℃ / 0.01 s^{-1}, 1000 ℃ / 0.1 s^{-1} and 900 ℃ / 0.001 s^{-1}. At 1000°C, it is noted that the experimentally determined recrystallization fraction increases from 0.737 to 0.952 as the strain rate decreases from 0.1 to 0.01 s^{-1} at 1000 ℃. At 900 ℃ / 0.001 s^{-1} the DDRX phase fraction was 0.96. It is also evident that the experimentally calculated recrystallization fraction and those predicted by the model are in reasonable agreement. The model prediction of DRX fraction is good at lower strain rate and underestimated at higher strain rate as the model assumes homogeneous deformation and do not considers flow localization. At high strain rates, flow localizations may accelerate DDRX in some regions and model do not account for this spatial variation.

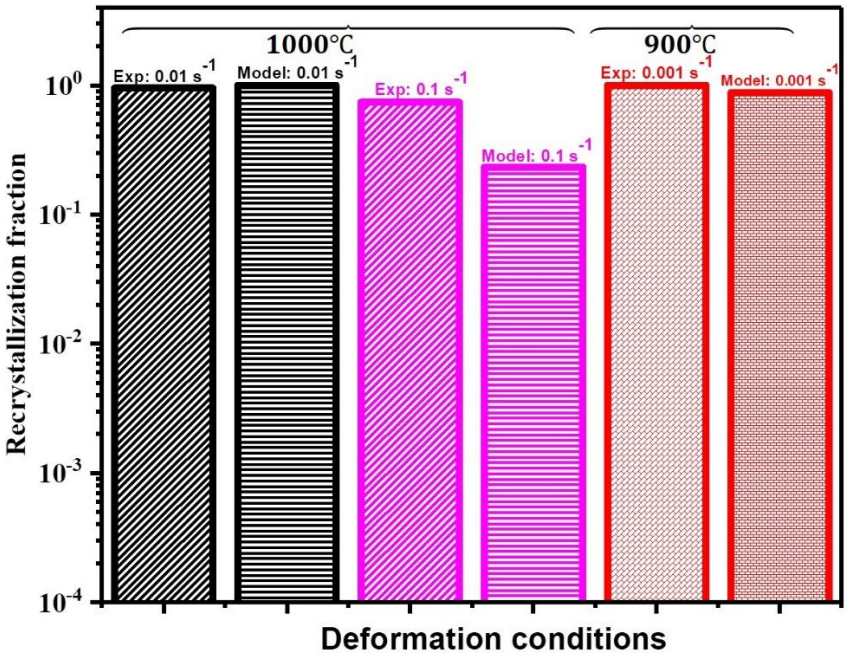

Figure 2.12. Comparison of simulated and experimentally measured recrystallization fraction (from GOS map) at the end of deformation for 1000 °C / 0.01 s^{-1}, 1000 °C / 0.1 $s^{-1}$and 900 °C / 0.001 s^{-1}.

2.5.3. Evolutions of dislocation density

Figures 2.13a and c, and Figures 2.13b and d depict the temperature and strain rate influences on the evolution of immobile and mobile dislocation density, respectively. ρ_i increases very fast during the onset of deformation and declines after reaching a peak value (see Figure 2.13a). With the strain, there is competition between SH, DRV and DDRX, reflected in the evolution of ρ_i. Initially, the material hardens due to the high production rate of immobile dislocations. After reaching a peak value for ρ_i, the DDRX takes over, and ρ_i decreases to minimize the stored energy and achieve a steady state. The peak values of ρ_i are temperature and strain rate dependent and shifted to higher strain, with decreasing temperature and increasing strain rate. It can also be observed that ρ_i has larger magnitudes at higher strain rates (see Figure 2.13b), due to the high operation frequency of the Frank-Read sources and simultaneous action of immobilizations. At

1000 ^{o}C, overall immobile dislocation density is predicted in the range of $1.90 \times 10^{13.0}$ m^{-2}- $1.17 \times 10^{14.0}$ m^{-2}, respectively, for 0.01 s^{-1} - 10 s^{-1}. The mobile dislocation density increases with increasing the strain at a constant temperature/strain rate (see Figure 2.13 c and d) due to the action of Frank-Read sources. The mobile dislocation density has lesser magnitude at higher temperature / lower strain rate due to dominance of softening. The mobile dislocation density was predicted in the range of $2.68 \times 10^{14.0}$ m^{-2} - $9.50 \times 10^{14.0}$ m^{-2}, respectively, at 1000 ^{o}C / 0.01 s^{-1} - 10 s^{-1}. Dislocation density data could be compared with nickel-based superalloys data compiled from the literature and shown in Table 2.5. It can be said that the predicted values are of one order of magnitude higher, due to different composition and testing conditions.

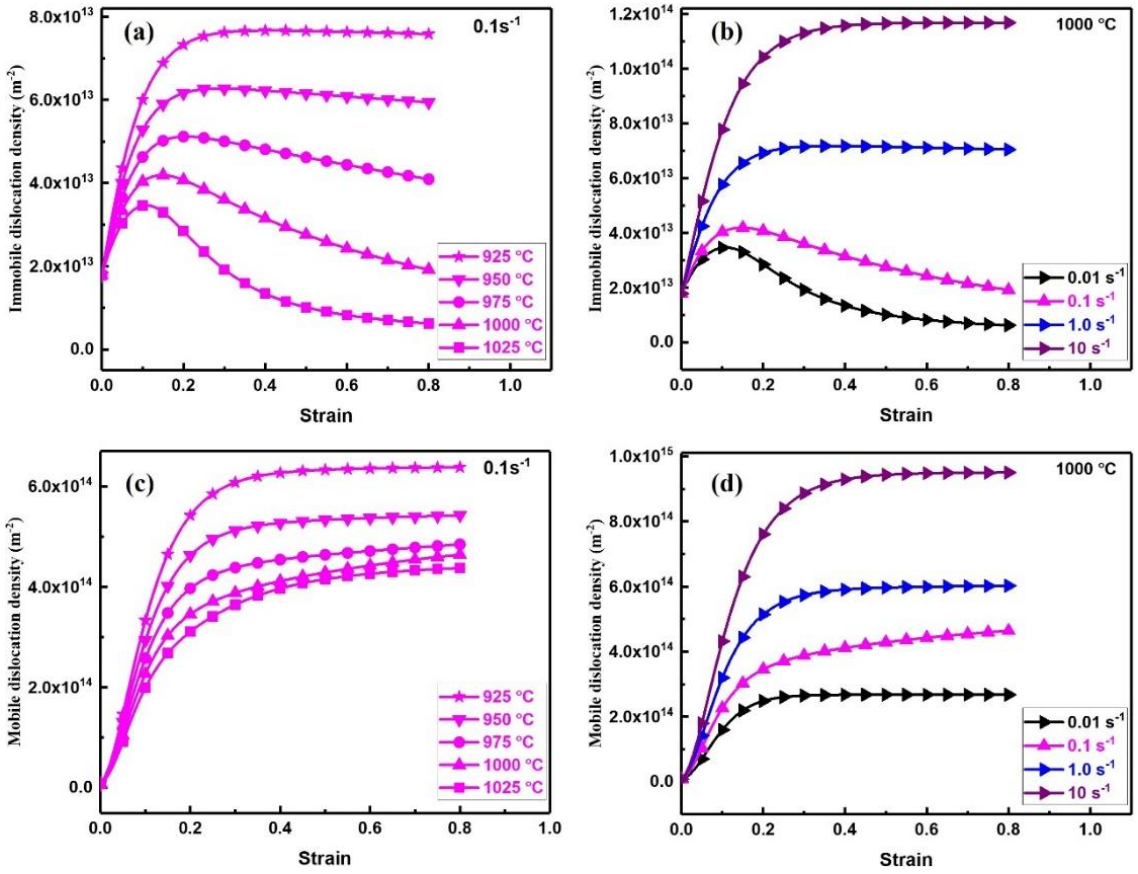

Figure 2.13. Evolutions of immobile and mobile dislocation density for IN718WP superalloy (a and c) 925 ^{o}C - 1025 ^{o}C / 0.1 s^{-1} and (b and d) 1000 ^{o}C / 0.01 s^{-1}- 10 s^{-1}.

Table 2.5. Dislocation density predicted in the literature at 0.8 strain

Material	Dislocation density	Conditions	Reference
Ni- based alloy	~ 4.0×10^{12} m^{-2}	1100 ℃ / 10^{-2} $s^{-1.}$	[30]
Ni- based alloy	~1.0×10^{13} m^{-2}	1100 ℃ / 10^{-1} $s^{-1.}$	[30]
Ni- based alloy	~2.0×10^{13} m^{-2}	1100 ℃ / 1 $s^{-1.}$	[30]

The boundary dislocation density obtained from EBSD and predicted immobile dislocation density were found to have affinity [41]. Immobile dislocations are relatively non-movable and may form dislocation entangles/cells and may give some small misorientation. From the EBSD misorientation data of small angle grain boundaries most of these dislocations can be quantified in terms of GNDs or sub boundaries dislocation density.

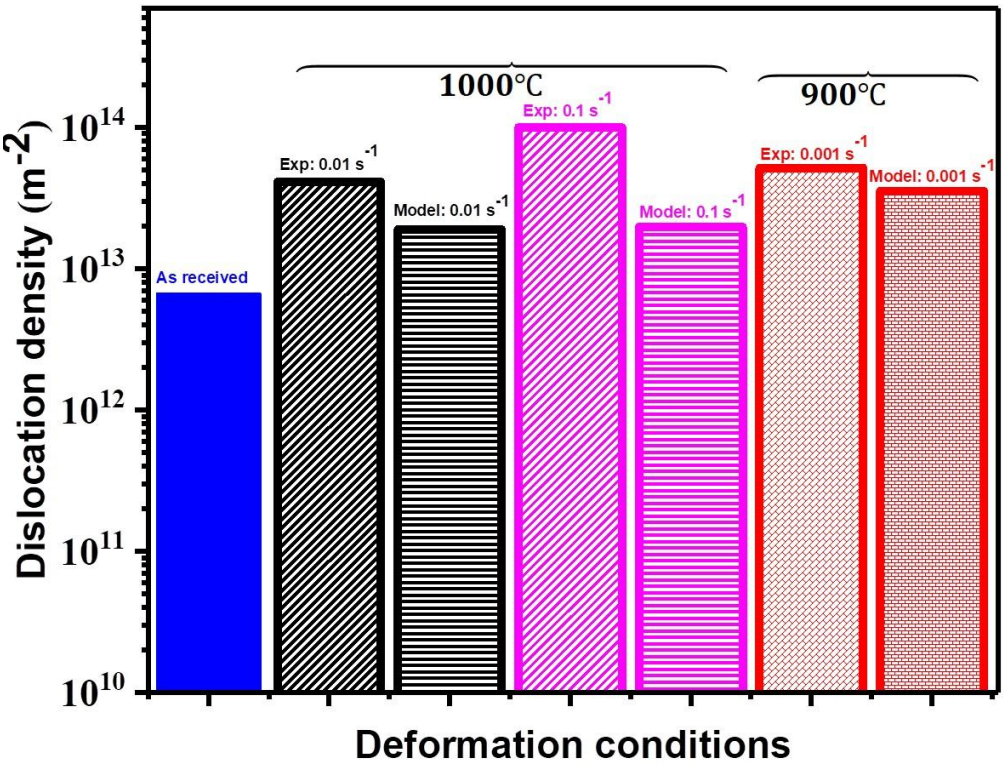

Figure 2.14. ρ_b calculated from EBSD data and ρ_i predicted from model for different conditions.

Hence a comparison between sub boundary dislocation density and immobile dislocation density can be done to validate the model. Average boundary dislocation density ρ_b was estimated from

EBSD data as per the method reported in the literature [97-99] and compared with the model predicted ρ_i in Figure 2.14. A reasonable agreement between the predicted and experimentally determined dislocation densities can be observed. The estimated magnitudes of ρ_b are about 4.12×10^{13} m^{-2} (at 1000 ℃ / 0.01 s^{-1}) and 1.01×10^{14} m^{-2} (at 1000 ℃ / 0.1 s^{-1}), respectively at 0.8 strain.

2.5.4. Glide velocities and climb velocities

Figures 2.15a, b and Figures 2.15c, d show the evolution of v_{gl} and v_{cl} predicted with this model. The glide velocity decreases with ongoing strain until reaching a steady state due to increased dislocation density and saturation. Furthermore, v_{gl} decreases with increasing the applied strain rate or decreasing temperature. These conditions promote more hardening corresponding to enhanced dislocation density, leading to a strong barrier for dislocation motion, see Figure 15a and b. The v_{gl} has a higher magnitude at higher temperatures or lower strain rates due to a weak barrier for dislocation motion. Higher glide velocity of dislocation is promoted due to occurrence of recrystallization phenomena at higher temperatures and lower strain rates. Climb velocity v_{cl} increases with the strain and then saturates at a steady state. With increasing strain rate and temperature, v_{cl} is observed to be increasing due to enhanced jump frequency of atoms and dislocation-mediated diffusional paths (see Figures 2.15c and d). At 1000 ºC, v_{gl} and v_{cl} are predicted in the range of $1.20 \times 10^{-4.0}$ ms^{-1} - 6.39×10^{-5} ms^{-1} and $3.21\times 10^{-10.0}$ ms^{-1}- $6.10 \times 10^{-10.0}$ ms^{-1}, respectively, for 0.01 s^{-1} - 10 s^{-1}. At 0.1 s^{-1}, v_{gl} and v_{cl} are predicted in the range of $1.57 \times 10^{-5.0}$ ms^{-1} – 1.55×10^{-4} ms^{-1} and $1.02 \times 10^{-10.0}$ ms^{-1} - $6.67 \times 10^{-10.0}$ ms^{-1}, respectively, for 925 ºC - 1025 ºC. It is reported that the dislocation velocity lies in the range of $\sim 3 \times 10^{-9}$ ms^{-1} - 3×10^{-4} ms^{-1} at 77 - 273K / 29.41-58.83 MPa in the stressed Ni single crystal [131]. No direct comparison can be made as the composition and testing conditions are different.

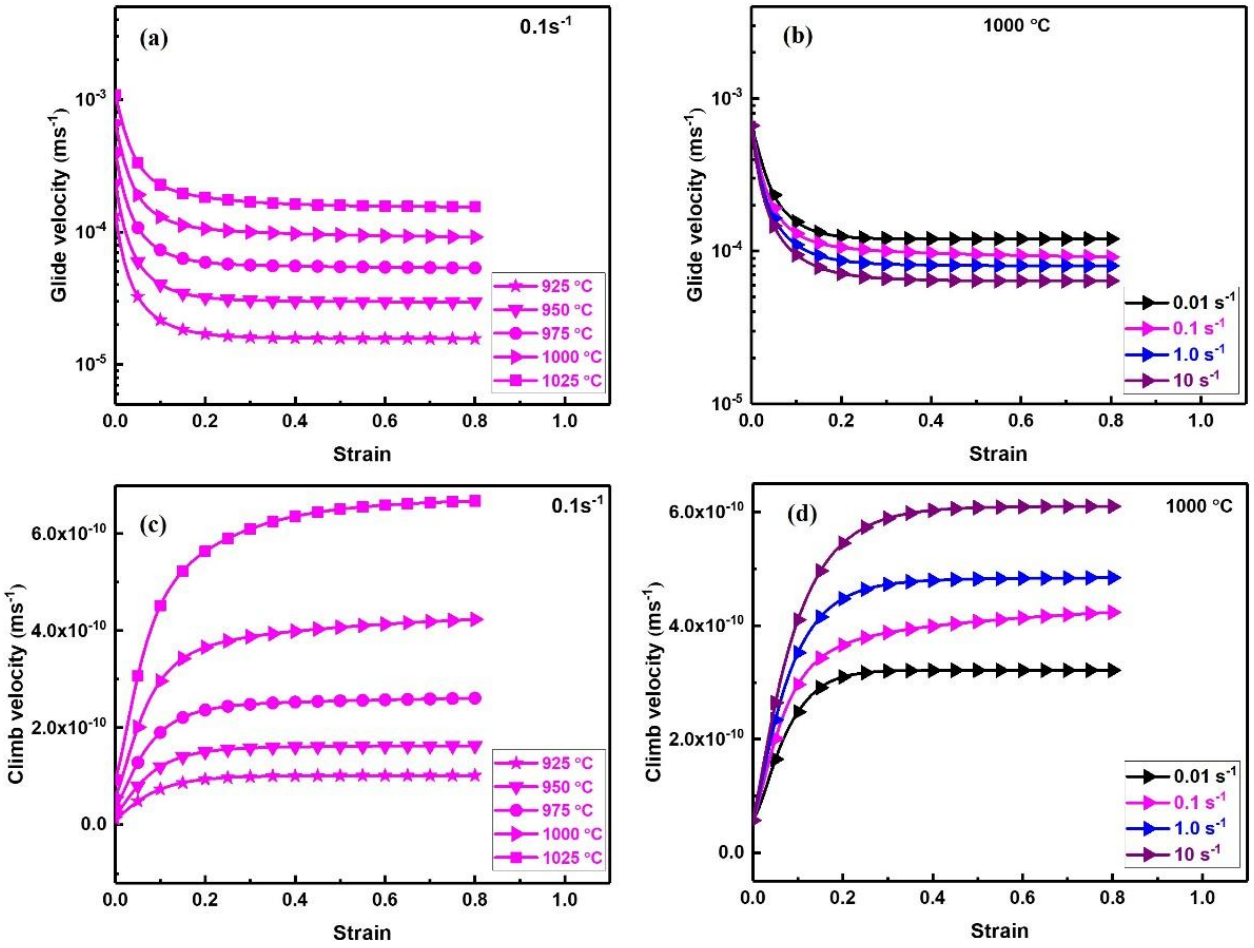

Figure 2.15. (a, c) Temperature effect on the v_{gl} and v_{cl} at 0.1 s^{-1}, (b, d) Strain rate effect on the v_{gl} and v_{cl} at 1000 ^{o}C.

Comparing the magnitudes of glide and climb velocities of dislocations, it may be deduced that the DDRX was facilitated more by dislocation glide. Finally, it can be said that this model can be also used for other similar alloys by providing the initial input parameters such as initial dislocation density and grain size along with only few curves. Its known that physically based models depend on microstructural ingredients that are highly dependent of the chemical composition and heat treatment. Desired set of parameters can be extracted from the optimization procedure explained in section 4 and rest of the curves can be easily predicted for any similar alloys.

2.6. Summary and Conclusions

The dislocation density-based flow stress model was developed by considering the physics behind DDRX phenomena to address the complete flow stress curve and microstructure evolution for the IN718WP superalloy. The model predicted the evolution of critical internal variables such as ρ_m and ρ_i and DDRX fraction with ongoing deformation. The model also demonstrates the evolution of dislocation velocities such as v_{gl} and v_{cl} in each time step of deformation. The effect of the strain rate and temperature on the flow stress curves was delineated employing model prediction and experimental data. Model capabilities for microstructure prediction were validated by comparing the results obtained with EBSD data in terms of dislocation density and DDRX fraction for reasonable range of deformation conditions that are relevant for industrial purposes. The advantage of the model is its ability to predict trends in how processing parameters affect the flow behaviour, with minimal computational effort and limited data. We conclude that:

- Recrystallized volume fraction was observed to be high at low strain rate or high temperature, observed through EBSD measurements and model predictions. The average grain size decreased and approached to steady state quickly at low strain rates or higher temperatures compared to higher strain rates or lower temperatures.
- Model predicted the increase in ρ_i during the onset of deformation followed by decline in magnitude due to dominance of DDRX followed by steady state at elevated temperatures or lower strain rates. The peak values of ρ_i were temperature and strain rate dependent and shifted to lower strain, increasing temperature and decreasing strain rate. Also, the peak values of ρ_i were increasing with decreasing temperature and increasing strain rate. Both ρ_i from the model and ρ_b from EBSD measurement exhibits analogous trends, showing an increase in magnitude with higher strain rates/ lower temperature.

- The mobile dislocation density increased with increasing the strain at a constant temperature/strain rate. ρ_m has lesser magnitude at higher temperature / lower strain rate due to dominance of softening. Estimated magnitude of ρ_m lies in the range of $6.38 \times 10^{14.0}$ - $4.37 \times 10^{14.0}$ m^{-2} and $2.68 \times 10^{14.0}$ m^{-2} - $9.50 \times 10^{14.0}$ m^{-2}, at 0.1 s^{-1}/ 925 ^oC - 1025 ^oC and 0.01 - 10 s^{-1}/ 1000 ^oC, respectively.
- Model output suggests that the higher climb and glide velocity of dislocations promoted the occurrence of recrystallization phenomena. As the applied strain rates increases or the temperature decreases, v_{gl} decreases. This is due to enhanced hardening caused by a rise in dislocation density, which acts as a stronger barrier against dislocation motion. vgl was predicted in the range of $1.57 \times 10^{-5.0}$ ms^{-1} – 1.55×10^{-4} ms^{-1} and $1.20 \times 10^{-4.0}$ ms^{-1} - 6.39×10^{-5} ms^{-1} for 925 ^oC - 1025 ^oC / 0.1 s^{-1} and 1000 ^oC/ 0.01 s^{-1} - 10 s^{-1}, respectively.

- As the strain rate and temperature increase, climb velocity of dislocation is observed to be increasing due to the accelerated jump frequency of atoms and ease of diffusion facilitated along dislocation paths. v_{cl} was predicted in the range of $1.02 \times 10^{-10.0}$ ms^{-1} - $6.67 \times 10^{-10.0}$ $ms^{-1}$and $3.21\times 10^{-10.0}$ ms^{-1}- $6.10 \times 10^{-10.0}$ ms^{-1} for 925 ^oC - 1025 ^oC / 0.01 s^{-1} and 1000 ^oC / 0.01 s^{-1} - 10 s^{-1}, respectively.
- Presented model is practically useful for analyzing experimental flow stress response, as the single set of parameters can be determined through fitting of only few experimental flow curves. Rest of the curves can be modeled through the obtained single set of parameters.

Appendix 2.A

Derivation of DDRX fraction

The volume of spherical DRX grain without any impingement with another DRX grain can be expressed as [73],

$$V = \frac{4}{3}\pi r^3 = \frac{4}{3}\pi(vt)^3 \qquad (2.A.1)$$

Corrosponding recrystallized fraction X_{DDRX} is estimated for spherical DDRX grain as,

$$X_{DDRX} = \frac{4}{3}\pi N v^3 \int_0^t t^3 dt = \frac{\pi}{3} N v^3 t^4 \qquad (2.A.2)$$

Equation 2.*A.2* is only limited to the small value of the recrystallization fraction and does not account for impingement. As the number of DDRX grains increases the the correction factor should be incorporated to compensate for the impingement. Thus, the modified equation for the estimation of recrystallization fraction is given as [73],

$$X_{DDRX} = 1 - exp\left(-\frac{\pi}{3} N v^3 t^4\right) \qquad (2.A.3)$$

Diffusion coefficient

$$D_s = 9.2 \times 10^{-4.0} e^{-Q_s/RT} \qquad (2.A.4)$$

Dynamic recrystallization coefficient

F_{drx} is the dynamic recrystallization coefficient used in Equation (2.23). Grain size, strain rate and temperature dependent F_{drx} is estimated by Equation (2.A.5) in this model and adopted from the research by [29, 64] for Ni-based superalloy.

$$F_{drx} = A_x g^{m_x} \left(\dot{\varepsilon} exp\left(\frac{Q_x}{RT}\right)\right)^{n_x}, \qquad (2.A.5)$$

where A_x, m_x, n_x *and* Q_x are the material parameters.